

Fourier Boundary Features Network with Wider Catchers for Glass Segmentation

Xiaolin Qin, *Senior Member, IEEE*, Jiacen Liu, Qianlei Wang, Shaolin Zhang, Fei Zhu, Zhang Yi, *Fellow, IEEE*

Abstract—Glass largely blurs the boundary between the real world and the reflection. The special transmittance and reflectance quality have confused the semantic tasks related to machine vision. Therefore, how to clear the boundary built by glass, and avoid over-capturing features as false positive information in deep structure, matters for constraining the segmentation of reflection surface and penetrating glass. We proposed the Fourier Boundary Features Network with Wider Catchers (FBWC), which might be the first attempt to utilize sufficiently wide horizontal shallow branches without vertical deepening for guiding the fine granularity segmentation boundary through primary glass semantic information. Specifically, we designed the Wider Coarse-Catchers (WCC) for anchoring large area segmentation and reducing excessive extraction from a structural perspective. We embed fine-grained features by Cross Transpose Attention (CTA), which is introduced to avoid the incomplete area within the boundary caused by reflection noise. For excavating glass features and balancing high-low layers context, a learnable Fourier Convolution Controller (FCC) is proposed to regulate information integration robustly. The proposed method has been validated on three different public glass segmentation datasets. Experimental results reveal that the proposed method yields better segmentation performance compared with the state-of-the-art (SOTA) methods in glass image segmentation.

Index Terms—Glass segmentation, FFT, boundary-constraint, cross transpose attention, wider coarse-catchers

I. INTRODUCTION

AS a solid, glass has special properties of both light transmission and reflection, hence it is widely used in many scenes, such as streets, buildings, and industrial production workshops. At the same time, due to prior knowledge and the complex visual nervous system, humans can detect the glass, what is behind the glass, and the reflected virtual world, which is a huge task for machines. To reduce the impact of glass on the practical tasks of intelligent systems based on machine vision (e.g., depth estimation and driving obstacle avoidance), machine vision is required to accurately segment the glass region.

Previous exploration of glass semantic segmentation consistently found boundary detection and context information

Xiaolin Qin, Jiacen Liu, Qianlei Wang, and Shaolin Zhang are with the Chengdu Institute of Computer Applications at Chinese Academy of Sciences, Chengdu, 610213, China. Email: qinxl2001@126.com, dreack-liu123552@163.com, wangqianlei36@gmail.com, z84489916@gmail.com

Xiaolin Qin, Qianlei Wang, and Shaolin Zhang are also with the School of Computer Science and Technology at University of Chinese Academy of Sciences, Beijing, 101408, China.

Fei Zhu is with the Centre for Artificial Intelligence and Robotics at Hong Kong Institute of Science & Innovation, Chinese Academy of Sciences, Hong Kong, 999077, China. Email: zhufei2018@ia.ac.cn.

Zhang Yi is with the School of Computer Science at Sichuan University, Chengdu, 610065, China. Email: zhangyi@scu.edu.cn.

Xiaolin Qin, Qianlei Wang, and Zhang Yi are the corresponding authors.

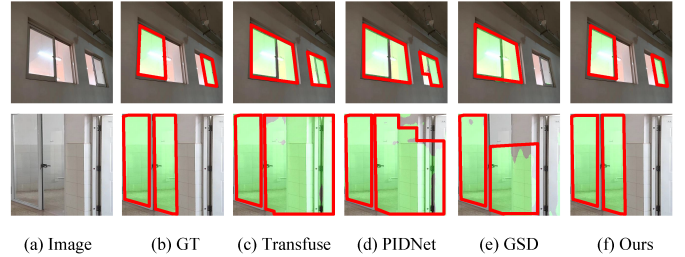


Fig. 1. Visual examples of glass segmentation. Compared with the SOTA methods, it can be concluded that the proposed network can accurately locate the segmentation boundary through a shallow feature capture framework and boundary constraints, and at the same time, the segmentation region is restricted within the boundary to avoid over-capturing and maintain regional consistency.

as two effective solutions. In some complex scenes, the glass only provides weak or incomplete boundaries, and the context content is highly confused by the glass transmission and reflection, resulting in reduced segmentation accuracy of networks. Although the advance of current methods to counter the ambiguous glass boundaries and incoherent contextual information, there are absence of excavating the essential challenges: (1) Overabundant semantic information: the deep complex backbone model can extract fine-grained information to enhance the segmentation object detail. However, over-capturing essentially mismatches the glass segmentation because light transmission causes a strong context consistency between internal and external segmented areas, which is not susceptible to the affinity of highly extracted features; (2) Shaky boundary constraints: current methods utilize various boundary detectors to preserve the outline and locate regions, such as the shallow-low features, which are fragile and easily affected by the subsequent gradual abstraction and fine-granularity of the network.

To alleviate the issues above, we designed the Fourier Boundary Features Network with Wider Catchers (FBWC), which is a shallow-width glass segmentation network with stable boundary constraints. First, we introduce a novel feature extraction backbone to solve the critical problem of semantic information over-capturing. Specifically, Wider Coarse-Catchers (WCC) consist of multiple Capturing Units (CUs) to provide earlier trough points in the encoding process than the traditional backbone. The structure of shallow and wide with connections of continuous CUs benefits glass coarse-grained region information extraction through a series of appropriate horizontal trough points. At the same time, we fully take advantage of decoding to embed strong and steady

boundary constraint information, which is concentrated significantly throughout the backbone without dispersiveness and distortion in highly abstracted processes. For another characteristic of glass, we designed Cross Transpose Attention (CTA) specifically to resist the impact of noise reflected by glass on the shallow layers through the focusing object area. Based on large and coarse-grained regions, progressively strengthened boundary constraints, and features complemented with high focusing, the Fourier Convolution Controller (FCC) is pointedly proposed to consolidate shallow boundaries with Fourier transform and flexibly balance that heterogeneous information by self-learning convolution paradigm. To sum up, our contributions are as follows:

- To the best knowledge, we might be the first attempt to design a wide and shallow backbone to combat over-capturing in the glass segmentation task. Besides, continuous, stable, and strong boundary constraints are fully leveraged throughout our WCC. For an extra supplement, Cross Transpose Attention is proposed to focus on details for keeping regional integrity and consistency.
- A learnable solution for utilizing the heterogeneous features to self-adjust and balance the fusion is innovatively provided, which provide an optimal combination of coarse-grained and fine-grained feature representations by embedding classical convolution theory. Meanwhile, the Fast Fourier Transform (FFT) is embedded to enhance the generated boundary features.
- Experimental results on three different public glass segmentation datasets show that the proposed FBWC outperforms previous SOTA methods. We further demonstrate the ability of our network to reveal the nature of segmentation tasks based on glass properties.

II. RELATED WORKS

A. Boundary Detection

From the perspective of bionics, one of the important bases for humans to judge glass-like objects is to find their boundary [1], which is a significant clue to help us divide reality and the virtual world transmitted and reflected by glass. Hence, the existing methods [2]–[4] have carried out a lot of work around the glass boundary detection and made great progress. Xie *et al.* [5] found that due to high contrast in the edge of the glass, boundary detection is prone to observe compared with content for being paired with human visual perception. Therefore, they proposed a novel network named TransLab to utilize the predicted boundary map for improving accuracy. He *et al.* [6] enhanced boundary learning for glass segmentation through the refined differential module and further edge-aware point-based graph convolution to establish a complete shape along the boundary. At the same time, Cao *et al.* [7] argue that boundaries with large smaller amounts, the boundary-related imbalance problem, adversely affect glass semantic performance, which is solved by designed FakeMix. However, the mentioned methods of glass boundary detection heavily rely on the quality or quantity of boundary features extracted and optimized by the network, which is a worrying process due to weakening, distortion, and even dispersion of boundary during

progressively abstracting. For this, Li *et al.* [8] optimized edge pixels by explicitly sampling under decoupled supervision for better consistency. Similarly, indirect boundary supervision through a single pathway is shaky and vulnerable to the erosion of high-dimensional semantic features. Inspired by previous works, we fully utilize boundary constraints directly with multiple supervision, aiming at offering firm and robust constraint features in the decoding process.

B. Context Features of Glass

The instability of boundary constraints and weakly blurred boundaries provided by glass in some complex scenes [9] limit the favorable influence of glass boundary detection methods on the accuracy of segmentation results. Therefore, the methods are gradually biased towards the study of how to efficiently leverage abundant context for glass segmentation from multi-scale features extraction focusing [4] [10], [11] and effective fusion [12], [13]. Yu *et al.* [14] have considered deep-layer features with more high-level semantics to be better at the location. Shallow layer features own larger spatial sizes with detailed low-level information instead. PGSNet is designed through progressively aggregating to avoid fusing these features naively. Hu *et al.* [15] proposed a ViT-based deep architecture to associate multi-layer receptive field features and optimize fusion results. Besides, due to the large and complete glass regions context, the attention mechanism is in full utilization. CAGNet [16] integrates two kinds of convolutional attention mechanisms with a Transformer head for deep-shallow feature analysis and fusion. Hou *et al.* [17] further introduce the Transformer encoder-decoder architecture to boost the usage of multi-levels of context information. Lin *et al.* [18] embed context correlation into the attention module to bridge contextual links among objects both spatially and semantically.

Although complex and deep network structures can abstract spatial semantic features on multi-scales to facilitate subsequent feature fusion, for the special segmentation target, glass, over-captured segmentation features will destroy the coherence of shallow information, making it difficult for the network to maintain the integrity of large-area segmentation. At the same time, the previous attention mechanism is more inclined to deal with multi-scale features with different depths and shallow features, and it fails to effectively match the width feature extraction framework to complete the shallow feature self-focusing task.

C. Architecture of networks

In the classical network structure, deeper layers benefit the network's ability to abstraction, which is conducive to the affinity for high-level object features and captures rich and complex semantic information. In addition to the problem of gradient disappearance or explosion [19] with deepening architecture, depth-based networks often fall into the dilemma of over-capturing for the task of semantic segmentation of glass. Specifically, most of the glass-like objects are a large area with a complete boundary and regular shape, hence over-abstraction of this information is harmful to improving the performance

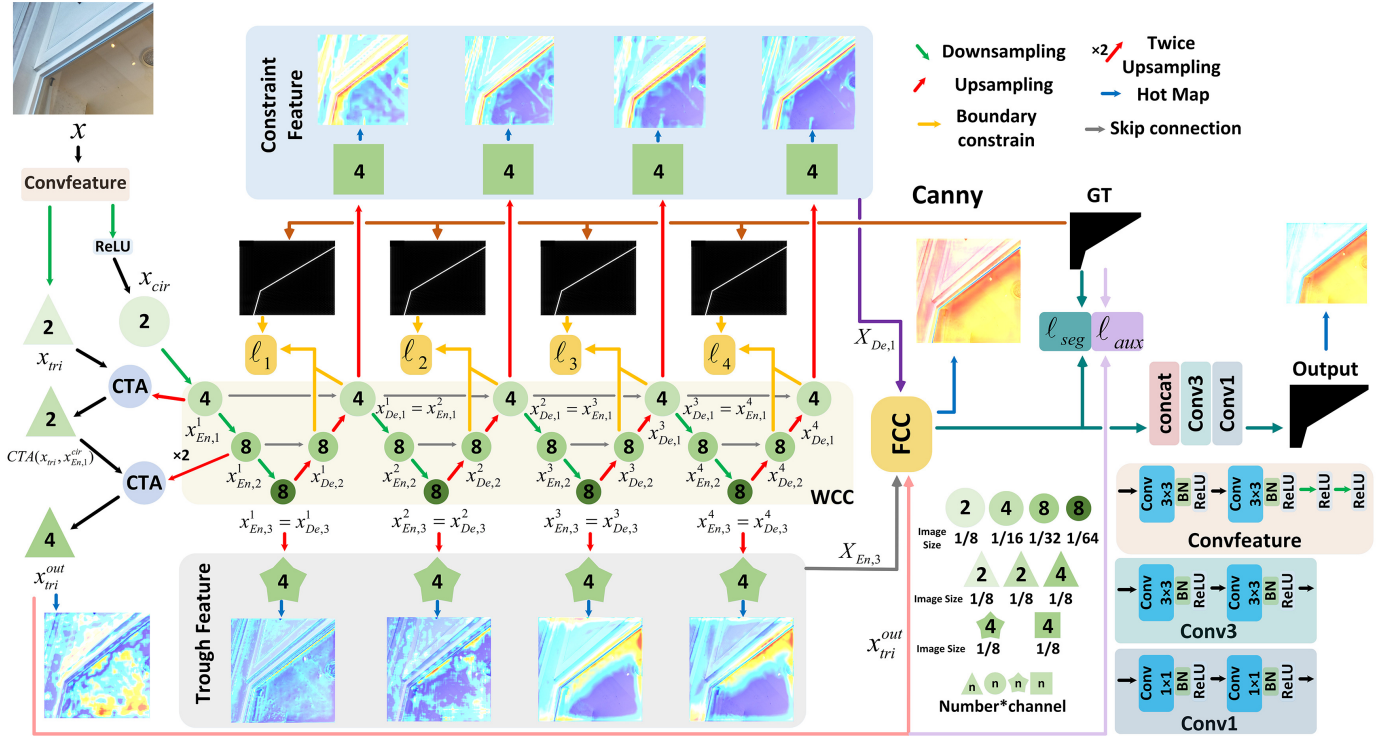


Fig. 2. Architecture of the proposed FBWC. Given an input glass image, there will be two branches to receive the same picture and change them into different features. In particular, one of features is fed into WCC to alleviate the over-capturing and boundary constraints of scarcity. The others is processed by the CTA to supplement and focus fine-grained information. The designed FCC as a learnable feature fusion regulator to balance heterogeneous inputs. Finally, a fine-grained weighting factor regulating the shallow and large area segmentation result with supplementing boundary information constraints to achieve the purpose of dynamic optimized network predictions.

of the segmentation. At the same time, the shallow features learning in the network can also learn the complex functions and information captured by the deep net [20]. Therefore, in order to better pair the object's characteristics of segmentation, a suitable network architecture with carefully balanced depth and width [21] is proposed to avoid the accuracy decrease caused by over-segmentation. Embracing the advantages of shallow layers, the basic low-level shape and outline of the glass can be relatively intact without distortion. Aiming at the reservation of shallow features, trough points, as turning points in the depth of the network, should occur in advance to avoid the dilution effect [22] of features during deepening. Inspired by the Broad Learning System [23]–[26], multiple trough points generated by the recurrent connections structure [27] widen the structure and drive the extracted information gradually permeating the network.

To mitigate the limitations associated with the conventional network framework in glass segmentation, such as overfitting from deep networks and the loss of intricate features from shallow networks, we propose a cyclic shallow backbone network. This network imposes rigorous constraints on layer-by-layer boundaries, enabling the extraction of semantic information tailored to the unique characteristics of the glass region. Thus, we attempt to explore the wider feature extraction to avoid over-capturing caused by a deeper network, which might be not suitable for the special semantic objects with large areas. This approach safeguards feature integrity and enhances

segmentation accuracy by ensuring that semantic information is effectively captured within the boundary range.

III. PROPOSED METHODOLOGY

The glass can be easily recognized by the human visual system based on prior knowledge, even though eyes suffer from the noise of objects through the glass and what the glass reflects. Humans are prone to utilize the surrounding context to confirm the existence of glass boundaries. With the information about the boundary, humans can accurately distinguish between the real world and the virtual world reflected by glass. This is particularly important for how machine vision circumvented the confusion of information brought by the properties of glass, both transmission and reflection. Inspired by this, we attempted to encode this practical phenomenon to achieve the bionic human visual system's intention to segment glass regions, then we proposed the FBWC.

A. Architecture

The overall architecture of the proposed FBWC is introduced in Figure 2. Firstly, for the input $x \in \mathbb{R}^{3 \times H \times W}$, we utilize downsampling and convolution operation as pretreatment to preliminarily obtain the same two features: $x_{tri} \in \mathbb{R}^{C \times \frac{H}{\lambda} \times \frac{W}{\lambda}}$ and $x_{cir} \in \mathbb{R}^{C \times \frac{H}{\lambda} \times \frac{W}{\lambda}}$ where C denotes the number of channels and λ downsampled shape hyperparameter.

For x_{cir} , we introduce WCC, which consists of I CUs, to acquire large and shallow information through lateral

broadening backbone without longitudinal deepening. Besides, the glass edge information extracted by the canny operator from ground truth is exploited to constrain the boundary in WCC. Then, CTA is for x_{tri} elaborated, which combines effective mechanism of attention between two feature branches to supplement and focus detailed information. Moreover, the core feature fusion regulator module of FBWC is designed as a FCC with a learnable paradigm to flexibly balance deep-shallow heterogeneous feature expression.

Based on the self-learning fusion feature controller, the FBWC derives a lot of adjustment flexibility and self-correction margin. Thus, instead of designing a complex loss function design, we introduce ohem cross-entropy and binary cross-entropy loss to monitor the propagation of semantic information across the proposed network. To be specific, for the i th decoder of CU in WCC, binary cross-entropy loss with boundary-awareness is applied by the Canny operator to gradually strengthen boundary constraints. At the same time, ℓ_{seg} and ℓ_{aux} refer to supervised learning from ground truth to the controller and attention mechanism results with ohem cross-entropy loss, respectively. Therefore, the final loss for FBWC is:

$$Loss = \ell_{seg} + \ell_{aux} + \frac{1}{I} \sum_{i=1}^I \ell_i. \quad (1)$$

B. Wider Coarse-Catchers

The point at both large segmentation and transmittance areas like the object of glass, we hold the opinion that over-capturing with classical deep structure embraces noise instead. Due to deep layers' highly abstracting semantic information, a backbone with a complex semantic concentration frame generates dispersive fine-grained features which make a barrier for boundary constraints and glass surface segmentation. Therefore, taking advantage of low-level semantic information in shallow layers is conducive to pairing the implicit characteristics of the glass.

As shown in Figure 3, we employ CUs as the component of our WCC. We notice that shallow encoded information can provide a large area of segmentation, and the decoding process is conducive to boundary constraints. Hence, the CU consists of three layers $l \in [1, 2, 3]$ encoding-decoding symmetric structure and three important points: start point, trough point, and end point. In particular, the constraint point is named by sharing the both start and end position in WCC.

Specifically, in the encoding process, we use convolution and down-sampling to double the number of channels and half the size of height and width respectively on each layer, which can be formulated as:

$$x_{En,l}^i = \Gamma^{l-1} \{ \omega \cdot \vartheta^{3 \times 3} (x_{En,1}^i) \}, l \in [2, 3], \quad (2)$$

where ω and $\vartheta^{3 \times 3}$ denote down-sampling and convolutional operator, respectively. And the $\Gamma^l\{\cdot\}$ is defined as the continuous operator which executes l times.

For the i th CU, $x_{En,3}^i$ or $x_{De,3}^i$ and $x_{En,1}^i$ are named trough point and start point, respectively. After the continuous operation of convolution and downsampling, in then process of decoding, we apply up-sampling operators with bilinear

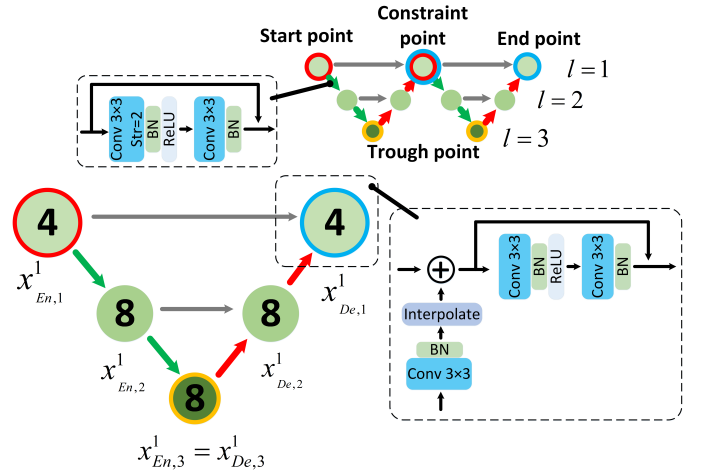


Fig. 3. Details of Capturing Unit on WCC, which is designed to avoid over-capturing and provide boundary constraint.

interpolation μ and the skip connection $S(\cdot)$ to bridge result features of up-sampling and $x_{En,l}^i$. Finally, the decoding process is defined as:

$$x_{De,l}^i = \vartheta^{3 \times 3} [S(\mu(x_{De,l+1}^i), x_{En,l}^i)], l \in [1, 2], \quad (3)$$

where $x_{De,l}^i$ denotes the features of the l th layer on the decoder of i th CU. And the operator of skip connection $S(\cdot)$ is defined as $S(a, b) = a \oplus b$. To sum up, the CU mapping (Ξ_{CU}) can be expressed as:

$$\Xi_{CU}(z) = S(\tilde{z}, \hat{z}), \quad (4)$$

where \tilde{z} and \hat{z} represent continuously downsampling-convolutional and upsampling-convolutional results based on the feature z , respectively. Furthermore, \tilde{z} is denoted as upsampling the results of \hat{z} . The process of input x_{cir} getting outputs after the first CU is formulated as:

$$\begin{bmatrix} x_{De,1}^1 \\ x_{En,3}^1 \end{bmatrix} = \Xi_{CU}(x_{cir}). \quad (5)$$

$x_{En,3}^1$ is for coarse-grained features acquisition and $x_{De,1}^1$ is for continuous asymptotic boundary constraints. Generally, when $i \in [1, 2, \dots, N]$, this means that multiple CUs need to be connected in series. As a result, the representation of variables on output layers in CUs are defined as following:

$$\begin{cases} x_{En,1}^i = \omega \cdot \vartheta^{3 \times 3} (x_{cir}), i = 1 \\ x_{En,1}^i = x_{De,1}^{i-1}, i \neq 1. \\ \begin{bmatrix} x_{De,1}^i \\ x_{En,3}^i \end{bmatrix} = \Gamma^i \{ \Xi_{CU}(x_{cir}) \}, others \end{cases} \quad (6)$$

Finally, the constraint points set $X_{De,1} = \{x_{De,1}^i\}_{i=1}^N$ and trough points set $X_{En,3} = \{x_{En,3}^i\}_{i=1}^N$ are represented as the outputs of multiple CUs for forming a wider shallow feature capture framework.

C. Cross Transpose Attention

Through WCC as backbone, trough point and constraint point gather large glass semantic region and strong constraint boundary information respectively to avoid over-capturing

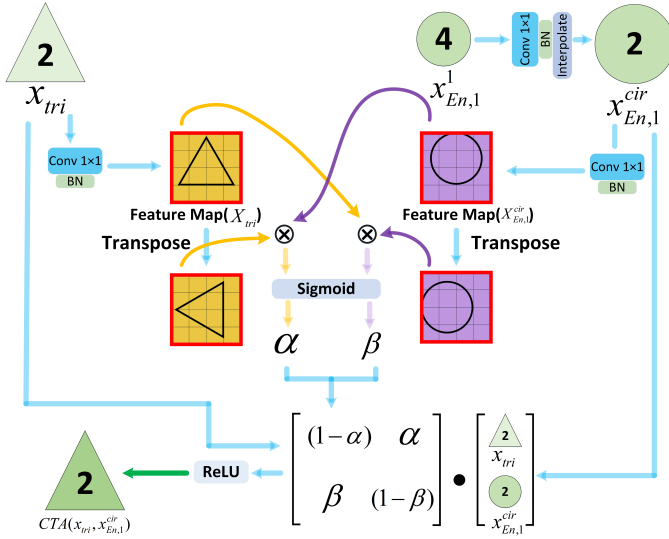


Fig. 4. Illustration of Cross Transpose Attention (CTA) blocks.

noise caused by the structure of trough point lagging. However, shallow and wide networks with early troughs are prone to suffer from unfocused features, which results in incomplete semantic regions within the boundary due to glass reflection. To supplement the fine-grained features and keep regional consistency, CTA is designed as an auxiliary branch for accurate segmentation, which is illustrated in Figure 4.

For the input x_{tri} , $x_{En,1}^1$ and $x_{En,2}^1$, we first keep the image size consistent through bilinear interpolation for obtaining $x_{En,1}^{cir}$ and $x_{En,2}^{cir}$. As for x_{tri} and $x_{En,1}^1$, mapping the same size tensors separately utilizing convolution: $X_{tri} = BN(\vartheta^{1 \times 1}(x_{tri}))$ and $X_{En,1} = BN(\vartheta^{1 \times 1}(x_{En,1}^1))$. Then, we transpose the respective tensors to cross multiply at the same pixel position for calculating the weight of the pixel. By the generated cross attention weights, a joint matrix is established to obtain updated attention results. We formulate the mentioned process:

$$\alpha = \sigma \left(X_{En,1}^{cir} \cdot X_{tri}^T \right), \quad (7)$$

$$\beta = \sigma \left(X_{tri} \cdot X_{En,1}^{cirT} \right), \quad (8)$$

$$CTA(x_{tri}, x_{En,1}^{cir}) = \begin{bmatrix} (1-\alpha) & \alpha \\ \beta & (1-\beta) \end{bmatrix} \cdot \begin{bmatrix} x_{tri} \\ x_{En,1}^{cir} \end{bmatrix}, \quad (9)$$

where σ refers to Sigmoid function and $CTA(a, b)$ is denoted as Cross Transpose Attention operator with tensors of a and b . The cross similarity coefficients are expressed by α and β . The final output of CTA is $x_{tri}^{out} = CTA((CTA(x_{tri}, x_{En,1}^{cir}), x_{En,2}^{cir}))$ for effective focusing on fine-grained semantic features.

D. Fourier Convolution Controller

Instead of directly fusing information among x_{tri}^{out} , $X_{En,3}$, and $X_{De,1}$, the FBWC utilizes FCC as the features learnable regulator to deal with heterogeneous inputs. Figure 5 illustrates the detailed structure of our FCC, which is designed to provide an optimal combination of coarse-grained and fine-grained

feature representations by embedding classical convolution theory. This feature combination is a nonlinear combination of features under different branches:

$$\arg \min_{\eta, \varpi, \xi} \left(Y - f_{\eta, \varpi, \xi} \left(g_1(x_{tri}^{out}), g_2(X_{En,3}), g_3(X_{De,1}) \right) \right), \quad (10)$$

where $g_1(\cdot)$, $g_2(\cdot)$, $g_3(\cdot)$ represent the feature extraction of three different branches under parameter sets (η, ϖ, ξ) , the $f(\cdot, \cdot, \cdot)$ means model training and output the feature after fusion, and the parameter sets (η, ϖ, ξ) are learnable. The Y represents the desired feature which determined by ground-truth. We use X^F to represent the result of $X_{En,3}$ fused with the glass edge information extracted through FFT:

$$X^F = \vartheta^{1 \times 1}(X_{En,3}) + \boxplus_{x_{En,3}^i} [F_{x_{En,3}}(c, d)], i \in [1, 2, 3, 4], \quad (11)$$

where the $\boxplus_{x_{En,3}^i} [\cdot]$ means executing operation for each channel of $x_{En,3}^i$ which belongs to $X_{En,3}$, and the $F_{x_{En,3}}(c, d)$ represents the glass edge information extracting process:

$$F_{x_{En,3}}(c, d) = \sum_{w=0}^{\frac{W}{\lambda}-1} \sum_{h=0}^{\frac{H}{\lambda}-1} x_{En,3}(w, h) e^{-j2\pi(\frac{\lambda cw}{W} + \frac{\lambda dh}{H})}, \quad (12)$$

where $c \in [0, \dots, \frac{W}{\lambda} - 1]$ and $d \in [0, \dots, \frac{H}{\lambda} - 1]$ refer to frequency domain variables. In the FFT process, the $x_{En,3}(w, h)$ is the value of the feature point at position (w, h) in one channel belongs to $x_{En,3}^i$.

Proposition 1. Assuming I^* is an image with regular geometric boundaries. For any continuous piecewise linear function subset Ω and any $f \in \Omega$, any convolutional neural network $f_J^{\mathbf{w}, \mathbf{b}}$ with depth $J \in \mathbb{Z}^+$ and ReLU function exists:

$$\|f - f_J^{\mathbf{w}, \mathbf{b}}(FFT(I^*).real + I^*)\|_{\Omega} < \|f - f_J^{\mathbf{w}, \mathbf{b}}(I^*)\|_{\Omega}. \quad (13)$$

Proof. The two-dimensional FFT can be regarded as a generalization of one-dimensional FFT, then we obtain expression of a single feature point value on a single column:

$$x_{En,3}(h) = \frac{a_0}{2} + \sum_{n=1}^P [a_n \cdot \cos(nwh) + b_n \cdot \sin(nwh)]. \quad (14)$$

We replace $\cos(nwh)$ and $\sin(nwh)$ by $(e^{inwh} + e^{-inwh})/2$ and $-i(e^{inwh} - e^{-inwh})/2$ respectively, then Eq.14 can be reformed as:

$$x_{En,3}(h) = \frac{a_0}{2} + \sum_{n=1}^P \left[\frac{a_n - ib_n}{2} \cdot e^{inwh} + \frac{a_n + ib_n}{2} \cdot e^{-inwh} \right]. \quad (15)$$

Let $c_0 = \frac{a_0}{2}$, $c_n = \frac{a_n - ib_n}{2}$, $c_{2P+1-n} = \frac{a_n + ib_n}{2}$, where $N = 2P + 1 = \frac{H}{\lambda} - 1$, $n \in [1, 2, 3, \dots, P]$, then we obtain a more unified form:

$$x_{En,3}(h) = c_0 \cdot e^{ihw \cdot 0} + c_1 \cdot e^{ihw \cdot 1} + c_2 \cdot e^{ihw \cdot 2} + \dots + c_{N-1} \cdot e^{ihw \cdot N-1}, w = 2\pi/N. \quad (16)$$

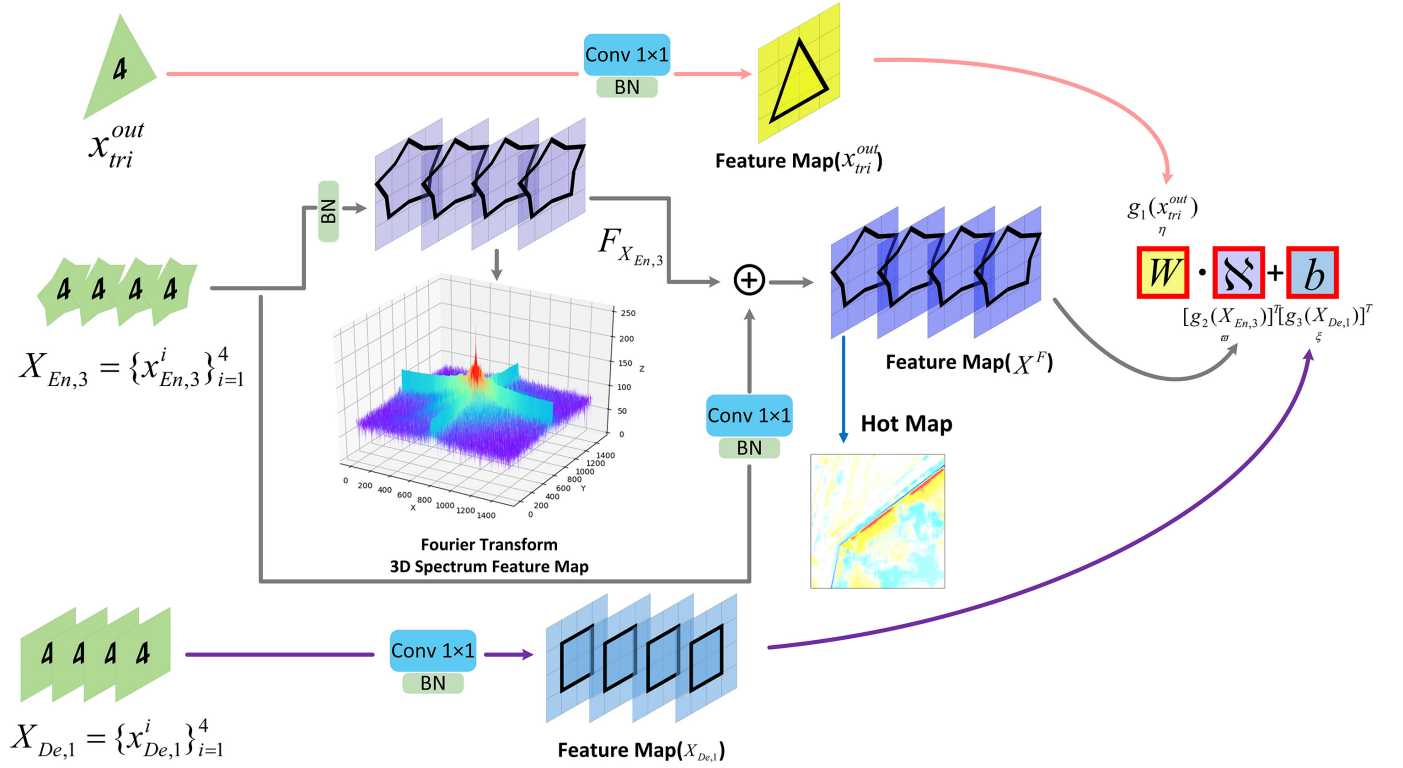


Fig. 5. Illustration of FCC, which serves as the core component of FBWC for providing a flexible solution to the features fusion problem.

The process of FFT can be thought of as the solution of the inverse of in the following equation:

$$\Theta \cdot \begin{bmatrix} c_0 \\ c_1 \\ c_2 \\ \vdots \\ c_{N-1} \end{bmatrix} = \begin{bmatrix} x_{En,3}(0) \\ x_{En,3}(1) \\ x_{En,3}(2) \\ \vdots \\ x_{En,3}(N-1) \end{bmatrix}, \quad (17)$$

where $\Theta =$

$$\begin{bmatrix} 1 & 1 & \dots & 1 \\ e^{iw \cdot 0} & e^{iw \cdot 1} & \dots & e^{iw \cdot (N-1)} \\ e^{i2w \cdot 0} & e^{i2w \cdot 1} & \dots & e^{i2w \cdot (N-1)} \\ \vdots & \vdots & \ddots & \vdots \\ e^{i(N-1)w \cdot 0} & e^{i(N-1)w \cdot 1} & \dots & e^{i(N-1)w \cdot (N-1)} \end{bmatrix}_{N \times N} \quad (18)$$

Then we use $\Theta^{-1}(j, k)$ to represent the element in j th row and k th column in Θ^{-1} , then c_j can be expressed as:

$$c_j = \sum_{k=0}^{N-1} x_{En,3}(k) \cdot \Theta^{-1}(j, k), j \in [0, 1, \dots, N-1]. \quad (19)$$

Let $j = j_{m-1} \cdot 2^{m-1} + \dots + j_v \cdot 2^v + \dots + j_1 \cdot 2 + j_0$, $k = k_{m-1} \cdot 2^{m-1} + \dots + k_v \cdot 2^v + \dots + k_1 \cdot 2 + k_0$, where $j_v = 0$ or 1 and $k_v = 0$ or 1 , and we define operation $[j_m, \dots, j_1, j_0]^*$ as follow:

$$[j_m, \dots, j_1, j_0]^* = j_m \cdot 2^m + \dots + j_1 \cdot 2 + j_0, \quad (20)$$

then we transfer Eq.19 into the following form:

$$c_{[j_{m-1}, \dots, j]^*} = \sum_{k_0} \sum_{k_1} \dots \sum_{k_{m-1}} x_{En,3}([k_{m-1}, \dots, k_0]^*) \cdot \Theta^{-1}(j, k_{m-1} \cdot 2^{m-1}) \cdot \Theta^{-1}(j, k_{m-2} \cdot 2^{m-2}) \dots \Theta^{-1}(j, k_0), \quad (21)$$

when $\Theta^{-1}(j, k_{m-1} \cdot 2^{m-1}) = \Theta^{-1}(j_0, k_{m-1} \cdot 2^{m-1})$, we can obtain the inner sum over k_{m-1} :

$$x_{En,3(l)}([j_0, \dots, j_{l-1}, k_{m-l-1}, \dots, k_0]^*) = \sum_{k_{m-1}} x_{En,3}([k_{m-1}, \dots, k_0]^*) \cdot \Theta^{-1}(j_0, k_{m-1} \cdot 2^{m-1}), \quad (22)$$

where l is the intercept location, if $l = 1, 2, \dots, m$, and $m = \log_2 N$, we can get a more general form:

$$x_{En,3(l)}([j_0, \dots, j_{l-1}, k_{m-l-1}, \dots, k_0]^*) = x_{En,3(l-1)}([j_0, \dots, j_{l-2}, k_{m-l-2}, \dots, k_0]^*) + (-1)^{j_{l-1}} \cdot i^{j_{l-2}} x_{En,3(l-1)}([j_0, \dots, j_{l-2}, k_{m-l-2}, \dots, k_0]^*) \cdot \Theta^{-1}(j_{l-3}, 2^{l-3} \cdot 2^{m-l}) \cdot \Theta^{-1}(j_{l-4}, 2^{l-4} \cdot 2^{m-l}) \dots \Theta^{-1}(j_0, 2^{m-l}). \quad (23)$$

From Eq.11 and Eq.23, the FFT result is shown as follow:

$$X^F = \vartheta^{1 \times 1}(X_{En,3}) + \boxplus_{x_{En,3}^i} \left[\sum_{w=0}^{\frac{W}{\lambda}-1} \sum_{l=1}^{\log_2 N} x_{En,3(l)} \right] \quad (24)$$

$, i \in [1, 2, 3, 4], l \in [1, 2, \dots, \log_2 N].$

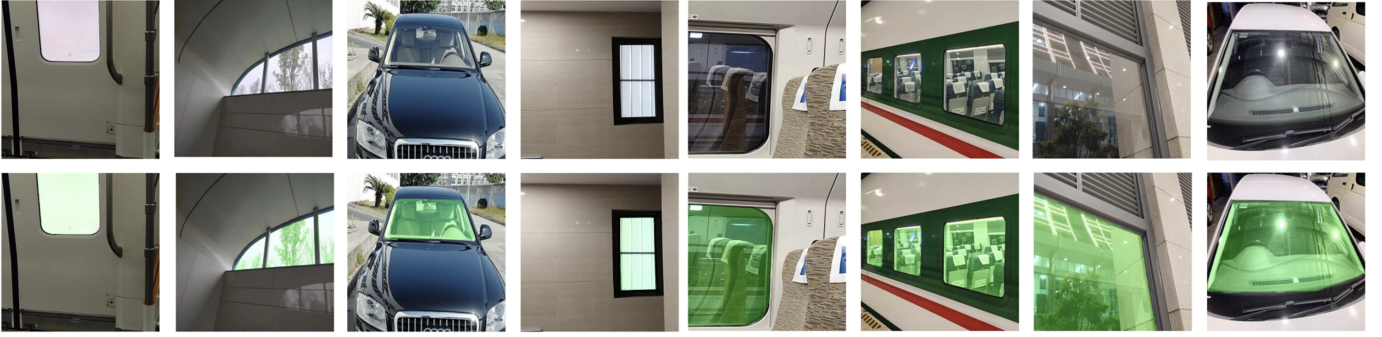


Fig. 6. More visual display of glass segmentation results of our FBWC beyond all the test sets.

In the above, it is evident that adjacent inner sums are subtracted with an interval of 1 during the process of conducting FFT, signifying the subtraction of feature point values within the complex domain. Due to the images have naturally sparse representations [28], we only use the even symmetry components of each channel, the real part is reserved. Then, feature points exhibiting significant differences will retain larger positive or negative values within the feature map tensor. Naturally, the influence of these negative values will be mitigated by the ReLU function. For convenience, we use a one-dimensional convolutional layer *Conv* to explain how FFT affects convolutional neural network learning.

Assuming the convolutional layer *Conv* has three neurons which share the weights W^* , the feature extraction process of convolution can be expressed as:

$$Input \cdot W^* = Output \cdot W^*, \quad (25)$$

where the *Input* comes from the output of the previous layer, and the *Output* is the features we want to extract. Specifically, what we want to obtain are boundary features, because the boundary features are crucial for glass segmentation. During network training, the correct weights W^* can map the specific values of the *Input* to more obvious values in *Output*. The loss function usually calculates the difference between the prediction value and the ground truth, but its essence is to calculate the errors between the ideal features and the extracted features by the network. We use \mathcal{E} and $\mathcal{N}_i (i \in [0, 1, 2])$ to represent the errors and neural nodes, then we obtain the relationship between errors and weights:

$$\frac{\delta \mathcal{E}}{\delta w_i} = \frac{\delta \mathcal{N}_0}{\delta w_i} \frac{\delta \mathcal{E}}{\delta \mathcal{N}_0} + \frac{\delta \mathcal{N}_1}{\delta w_i} \frac{\delta \mathcal{E}}{\delta \mathcal{N}_1} + \frac{\delta \mathcal{N}_2}{\delta w_i} \frac{\delta \mathcal{E}}{\delta \mathcal{N}_2}, w_i \in W. \quad (26)$$

The \mathcal{E} depends on the tensor values difference between the *Output* and the *Input*. If the tensor values of the *Input* are close to the *Output*, the \mathcal{E} will be more minor, then the fewer times it will take to update W . Since FFT extracts the edge information of the feature map, when the edge information is fused with the original feature map, the tensor values errors will be more minor. Due to convolution is a stretching of the original image, the original image I^* also satisfies the above explanation, the Proposition 1 is proved.

According to the $g_1(x_{tri}^{out})$ as weight branch W , the $g_2(X_{En,3})$ as variable branch \aleph and the $g_3(X_{De,1})$ as bias

branch b , we formally define learnable Fourier Convolution Controller as:

$$FCC = g_1(x_{tri}^{out}) \cdot [g_2(X_{En,3})]^\aleph + [g_3(X_{De,1})]^\xi. \quad (27)$$

In the FCC, the x_{tri}^{out} leads and magnifies the significance of fine-grained focusing regions based on shallow and large objects in $X_{En,3}$ without over-capturing, besides $X_{De,1}$ utilizes the boundary constraint feature to flexibly correct and limit the position of semantic regions.

IV. EXPERIMENTS

A. Experiment Setting

Datasets. For the performance evaluation of the proposed method, we carry out detailed experiments on three glass segmentation tasks: GDD [9], HSO [14], and Trans10K-Stuff [5]. To provide further clarity, the GDD comprises a total of 3916 images. Among these, 2980 images are allocated to the train set, while the remaining 936 images constitute the test set. Simultaneously, HSO serves as a comprehensive scene segmentation dataset, primarily focusing on family environments. It is meticulously crafted to unlock a myriad of applications for domestic robots. The dataset divided 3070 of 4852 images into a training set and 1782 as a test set. Aiming at exploring the glass segmentation task, in the selection of the data set, we prefer to choose the segmented transparent glass targets. Thus, on the large-scale transparent object segmentation dataset Trans10K-Stuff, which contains two categories: stuff and things, we utilize the category of stuff in the whole dataset. The filtered result dataset Trans10K-Stuff consists of 2455 train set and 1771 test set. For training, input images are augmented by randomly horizontal flipping and resizing. Throughout the testing process, all datasets of images are resized into 352×352 without any pre-processing.

Evaluation Metrics. The evaluation metrics used in the experiments for comparison of our proposed methods with other SOTA methods including, intersection over union (IoU), mean absolute error (MAE), and balanced error rate (BER), which are defined as follows:

$$IoU = \frac{TP}{TP + FP + FN}, \quad (28)$$

TABLE I

QUANTITATIVE COMPARISON TO THE STATE-OF-THE-ART METHODS ON THE DATASETS OF GDD [9], TRANS10K-STUFF [5] AND HSO [14]. ALL THE METHODS ARE RE-TRAINED ON THE CORRESPONDING TRAINING SET. ●: SEMANTIC SEGMENTATION METHODS. ○: SALIENT OBJECT DETECTION METHODS. △: SHADOW DETECTION METHODS. §: MEDICAL IMAGE SEGMENTATION METHOD. *: CAMOUFLAGED OBJECT DETECTION ▲: MIRROR SEGMENTATION METHODS. ◇: TRANSPARENT OBJECT SEGMENTATION METHODS. ✱: GLASS SEGMENTATION METHODS. THE FIRST AND SECOND BEST RESULTS ARE MARKED IN RED AND BLUE, RESPECTIVELY. OUR METHOD ACHIEVES THE BEST PERFORMANCE ON ALL THREE CHALLENGING DATASETS UNDER THREE STANDARD METRICS.

Methods	Pub.' Year	GDD			Trans10K-stuff			HSO		
		Trainset:2980 Testset:936		BER↓	Trainset:2455 Testset:1771		BER↓	Trainset:3070 Testset:1782		BER↓
		IoU↑	MAE↓		IoU↑	MAE↓		IoU↑	MAE↓	
ICNet●	ECCV'18	69.78	0.163	15.93	75.02	0.108	10.88	62.38	0.163	17.01
PSPNet●	CVPR'17	84.29	0.082	8.73	87.97	0.042	5.40	77.74	0.092	10.48
DeepLabv3+●	ECCV'18	70.06	0.142	15.21	51.66	0.224	23.75	64.69	0.146	15.97
DenseASPP●	CVPR'18	83.75	0.078	8.61	86.49	0.048	6.10	76.01	0.092	11.28
BiSeNet●	ECCV'18	80.31	0.102	10.99	85.95	0.054	6.08	75.97	0.100	11.02
DANet●	CVPR'19	84.28	0.086	8.89	88.26	0.043	5.21	77.78	0.090	10.54
CCNet●	ICCV'19	84.37	0.083	8.61	88.29	0.042	5.10	78.26	0.089	10.30
GFFNet●	AAAI'20	82.41	0.855	9.11	69.29	0.143	14.19	77.34	0.094	9.69
SFNet●	ECCV'20	81.04	0.101	10.18	71.34	0.130	13.08	77.59	0.088	10.68
FaPN●	ICCV'21	86.77	0.060	5.63	89.12	0.041	4.76	78.16	0.086	9.48
PIDNet●	CVPR'23	87.42	0.061	5.58	77.68	0.094	9.27	79.87	0.082	9.47
DSS○	TPAMI'19	80.24	0.123	9.73	84.77	0.075	6.42	73.08	0.135	12.04
PiCANet○	CVPR'18	83.74	0.093	8.24	83.99	0.077	7.03	71.66	0.148	13.31
RAS○	ECCV'18	81.05	0.104	9.43	85.48	0.061	6.17	74.76	0.113	11.18
CPD○	CVPR'19	82.62	0.092	8.81	86.14	0.060	5.85	76.24	0.108	10.49
EGNet○	ICCV'19	85.11	0.081	7.39	84.64	0.065	6.51	74.37	0.116	11.55
F ³ Net○	AAAI'20	84.87	0.078	7.33	86.37	0.058	5.78	76.95	0.102	10.53
MINet-R○	CVPR'20	82.17	0.089	8.49	85.94	0.059	6.01	76.65	0.104	10.27
ITSD○	CVPR'20	83.90	0.082	7.68	85.62	0.062	6.23	74.42	0.120	11.36
LDF○	CVPR'20	83.36	0.085	7.99	84.53	0.067	6.65	76.97	0.102	10.61
U2-Net○	PR'20	84.37	0.082	8.54	87.91	0.047	5.08	72.83	0.121	12.41
DSC△	CVPR'19	83.56	0.090	7.97	86.37	0.058	5.31	71.93	0.128	13.11
DSD△	CVPR'19	85.54	0.071	7.17	86.22	0.052	5.57	76.49	0.101	11.07
BDRAR△	ECCV'18	80.01	0.099	9.87	85.00	0.061	6.04	75.32	0.103	11.13
PraNet§	MICCAI'20	82.06	0.098	9.33	87.15	0.058	5.31	71.93	0.128	13.11
U-Net§	MICCAI'15	75.44	0.136	11.16	70.95	0.135	13.82	60.23	0.201	20.88
Transfuse§	MICCAI'21	81.78	0.092	9.68	88.6	0.042	4.81	77.6	0.108	10.07
SINet*	CVPR'20	79.28	0.133	10.14	85.01	0.064	6.37	76.07	0.113	10.92
PFNet*	CVPR'21	85.96	0.072	6.50	85.68	0.059	5.97	76.79	0.109	10.38
RankNet*	CVPR'21	84.54	0.085	7.70	86.55	0.055	5.77	76.88	0.105	10.59
MirrorNet▲	ICCV'19	85.07	0.083	7.67	88.30	0.047	4.95	78.82	0.102	9.93
PMD▲	CVPR'20	87.12	0.066	5.97	88.10	0.047	5.02	80.31	0.089	8.81
TransLab◇	ECCV'20	81.67	0.096	9.69	87.11	0.051	5.44	74.32	0.123	12.00
Trans2Seg◇	IJCAI'21	84.65	0.074	7.32	75.01	0.122	10.66	78.06	0.092	9.59
GDNNet*	CVPR'20	87.64	0.063	5.61	88.72	0.045	4.71	78.84	0.092	9.28
GSD*	CVPR'21	87.62	0.065	5.88	89.71	0.041	4.49	78.95	0.099	9.70
EBLNet*	ICCV'21	84.85	0.079	7.60	89.92	0.047	4.29	79.21	0.094	9.48
PGSNet*	IEEE TIP'22	87.81	0.062	5.56	89.79	0.042	4.39	80.06	0.089	9.08
RFENet*	IJCAI'23	77.74	0.118	10.90	81.60	0.082	8.17	65.43	0.152	15.09
FBWC	Ours	93.17	0.035	4.03	89.74	0.040	4.51	87.59	0.059	6.27

$$MAE = \frac{1}{H \times W} \sum_{(x,y)}^{(H,W)} |o(x,y) - l(x,y)|, \quad (29)$$

$$BER = 100 \times \left(1 - \frac{1}{2} \left(\frac{TP}{N_p} + \frac{TN}{N_n} \right) \right), \quad (30)$$

where the value of true-positive is denoted as TP, false-positive as FP, true-negative as TN, and false-negative as FN respectively. Simultaneously, $o(x,y)$ is denoted as the output of models for glass prediction and $l(x,y)$ represents the labels of annotation on the pixel (x,y) . N_p and N_n represent pixels in the images that contain and do not contain the segmented objects of glass, respectively.

Implementation Details. The method outlined in our paper is implemented using the PyTorch framework on an NVIDIA RTX 4090 GPU equipped with 24GB memory. The three public glass segmentation datasets are optimized using an SGD optimizer with a weight decay of 5×10^{-4} , an initial

learning rate of 0.001, and a momentum of 0.9. Throughout the training process, we utilize the polynomial learning rate policy to gradually adjust the initial learning rate, denoted as $(1 - \frac{iter}{max_iter})^{0.9}$.

B. Comparison Results

In this study, to verify the effectiveness and robustness of the proposed method for the task of glass segmentation, the method is compared with a variety of methods in several related fields with few glass segmentation methods at present. We conduct extensive experiments to compare the segmentation performance of our work and state-of-the-art methods including PraNet [29], U-Net [30], and Transfuse [31] on medical image segmentation methods. DSS [32], PiCANet [33], RAS [34], CPD [35], EGNet [36], F3Net [37], MINet-R [38], ITSD [39], LDF [40] and U2-Net [41] on salient object detection methods. ICNet [42], PSPNet [43], DeepLabv3+

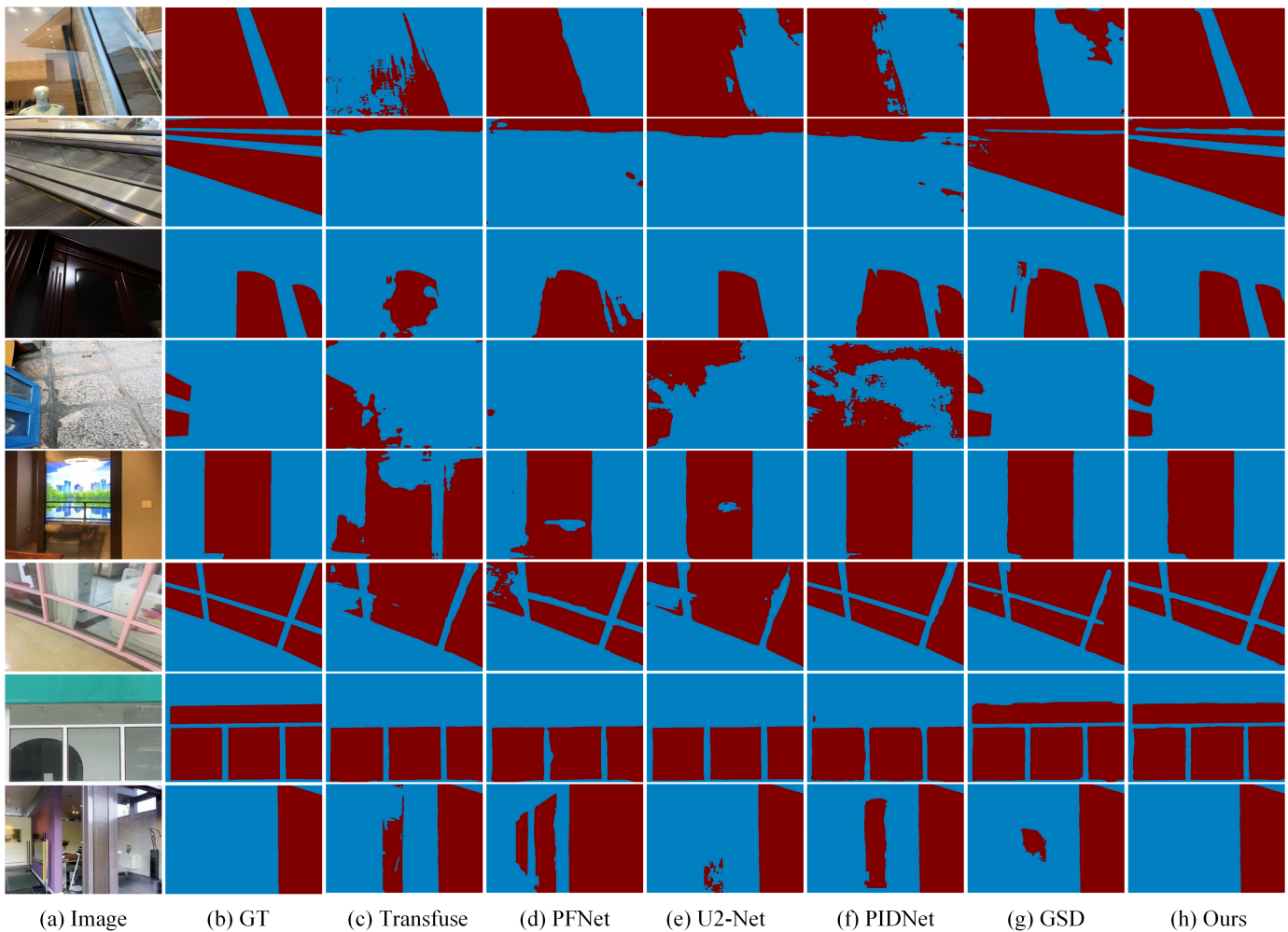


Fig. 7. Visual comparison of our FBWC with state-of-the-art methods.

[44], DenseASPP [45], BiSeNet [46], DANet [47], CCNet [48], GFFNet [49], SFNet [50], FaPN [51] and PIDNet [52] on semantic segmentation methods. DSC [53], DSD [54], and BDRAR [55] on shadow detection methods. SINet [56], PFNet [57], and RankNet [58] on camouflaged object detection methods. MirrorNet [59] and PMD [1] on mirror segmentation methods. TransLab [5] and Trans2Seg [60] on transparent object segmentation methods. GDNet [9], GSD [2], EBLNet [6], PGSNet [14], and RFENet [61] on glass segmentation methods. To be fair, we retrain their open codes on the three datasets for effective comparison.

Our quantitative results on the glass segmentation task achieve excellent performance compared to other 39 previous works on three benchmark datasets, which is present in Table I. The proposed method achieves the best comprehensive performance and surpasses the SOTA method PGSNet [14] on GDD with a significant improvement of IoU by 5.36%, a decrement of MAE and BER by 0.025 and 1.53 respectively. Besides, the proposed method shows a slight advantage on Trans10K-stuff with MAE and can be consistent with the SOTA methods on other metrics. At the same time, we can also see that FBWC outperforms the previous works on all

metrics based on HSO. Specifically, FBWC achieves 87.59% on IoU, 0.059 on MAE, and 6.27 on BER, which are 7.28% higher, 0.023 and 2.54 lower than the performance of the best glass segmentation method. From the test indexes of the three data sets, our FBWC comprehensively embodies excellent segmentation performance and generalization ability.

In addition to quantitative comparisons, from the visual qualitative results in Figure 7, we can observe that our FBWC can first fully constrain the boundary information of the segmented target region so that the visual results embrace a clear and complete segmentation boundary to distinguish the background and the glass region. Besides, our work relies on the advantages of shallow space acquisition structures to efficiently avoid the impact of over-capturing as noise on segmentation results. Finally, by establishing a semantic association between fine-grained feature focusing and large-area target region, the proposed method can accurately anchor the segmentation region to eliminate interference information.

C. Ablation Study

To evaluate the ability of horizontal shallow branches in the glass segmentation task to avoid excessive extraction

TABLE II
QUANTITATIVE ABLATION RESULTS AMONG DIFFERENT NUMBERS OF CUs. THE BASE-X MEANS FBWC WITHOUT WCC.

Datasets	Methods		Results		
			IoU \uparrow	MAE \downarrow	BER \downarrow
HSO	A	Base-X + 1 UC	78.98	0.099	9.85
	B	Base-X + 2 CUs	80.76	0.088	9.29
	C	Base-X + 3 CUs	81.27	0.080	8.97
	D	Base-X + 4 CUs	87.59	0.059	6.27
	E	Base-X + 5 CUs	80.22	0.092	9.35
Trans10K-stuff	A	Base-X + 1 CU	78.54	0.082	8.87
	B	Base-X + 2 CUs	80.33	0.079	7.85
	C	Base-X + 3 CUs	85.71	0.061	6.24
	D	Base-X + 4 CUs	89.74	0.040	4.51
	E	Base-X + 5 CUs	82.39	0.072	6.86
GDD	A	Base-X + 1 CU	88.38	0.062	5.58
	B	Base-X + 2 CUs	89.01	0.061	5.47
	C	Base-X + 3 CUs	90.52	0.058	5.38
	D	Base-X + 4 CUs	93.17	0.035	4.03
	E	Base-X + 5 CUs	87.89	0.071	5.70

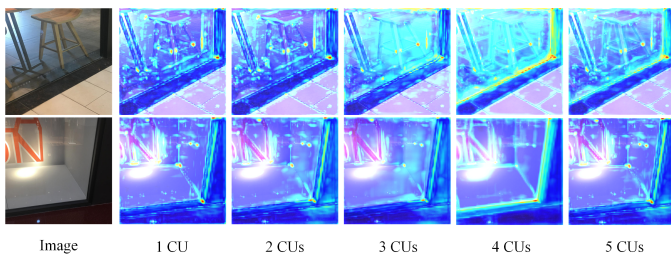


Fig. 8. Heat maps from different numbers of CUs.

and the influence of various components of our proposed FBWC, we further conduct ablation studies on three datasets, which can verify the effectiveness and generalization ability of designed factors in the model. Firstly, we design WCC against the phenomenon of over-capturing. With the increase of the depth of the network structure, semantic information will be gradually abstracted, and excessive detail noise will be prone to be introduced in the glass segmentation situation, which is not conducive to the complete acquisition of large-area targets. Due to the disadvantages of vertical structure, we concatenate CUs horizontally to avoid excessive abstraction of glass information. At the same time, the amount of CUs in the transverse connection process will also affect the experimental results. Therefore, we conducted ablation experiments on the numbers of CUs to determine the optimal quantity.

Based on Table II, we can observe a positive increase in all three evaluation metrics with the increment of CU numbers. This trend underscores the significance of the WCC within our FBWC, which comprises four distinct CUs. Within each CU, boundary constraints are introduced to ensure clear partition edges. Therefore, in the process of the gradual increase of the number of CUs, the continuous strengthening of constraints and the effective transfer of accumulated shallow information lead to improved segmentation results. However, this horizontal information transfer will lead to the last CU retaining miscellaneous information without providing more effective semantic information, and lead to lower segmentation accuracy.

It can be seen from the heat map that with the increase

TABLE III
QUANTITATIVE ABLATION RESULTS AMONG DIFFERENT LAYERS OF TROUGH POINT.

Datasets	Methods		Results		
			IoU \uparrow	MAE \downarrow	BER \downarrow
HSO	A	the second layer	78.64	0.101	10.07
	B	the third layer	87.59	0.059	6.27
	C	the fourth layer	81.52	0.078	8.81
Trans10K-stuff	A	the second layer	75.26	0.106	9.34
	B	the third layer	89.74	0.040	4.51
	C	the fourth layer	80.76	0.077	7.79
GDD	A	the second layer	87.22	0.067	5.71
	B	the third layer	93.17	0.035	4.03
	C	the fourth layer	87.02	0.068	5.78

in the number of CUs, the boundary constraints continue to strengthen, which is expressed in the Figure 8 as the segmentation boundary gradually becomes obvious. When the number is from 4 to 5, the boundary constraints will degenerate due to the interference of redundant information. Based on the quantitative results from the numbers 4 to 5, we prudently chose 4 as the optimal number to balance the effects of boundary constraint validity and semantic information redundancy on segmentation results.

Considering the vertical structure, in the CU, we design a trough point on the third layer for properly capturing spatial information without further deepening. To verify the appropriateness of the occurrence of trough points, trough points on different layers are designed into the ablation experiment.

As shown in Table III, trough points on the second layer under the three datasets perform worse than the other experimental groups based on a small number of convolutions. Therefore, the advanced appearance of the trough point will cause WCC to over-capture shallow semantic information and fail to excavate the intra-class consistency features without further abstraction. By contrast, when extending and deepening trough points into the fourth layer, the segmentation performance of the model is negatively affected by multi-layer convolution to over-abstracting dispersive fine-grained features as noise. In general, faced with the glass segmentation task, an appropriate trough point can capture the commonalities among glass classes through the appropriate convolution quantity while avoiding the difficulty of feature clustering and the decrease of semantic relevance caused by excessive extraction. Similarly, the proposed CTA and FCC are also considered in the ablation experiment to verify the validity of the designed attention mechanism and Fourier enhancement for glass features.

Based on Table IV, we observe that the segmentation performance on all three datasets decreased without CTA to supplement the focused semantic features and maintain the integrity of semantic information in the edge constraint region. From Figure 9, it can be vividly seen that CTA can effectively filter the reflected strong light noise, fully focus the semantic information in the target region and reduce the dispersion of segmentation results. At the same time, we introduce the Fourier Transform on a variable branch to FCC, which is conducive to further strengthening the boundary information, increasing the boundary sensitivity of the model,

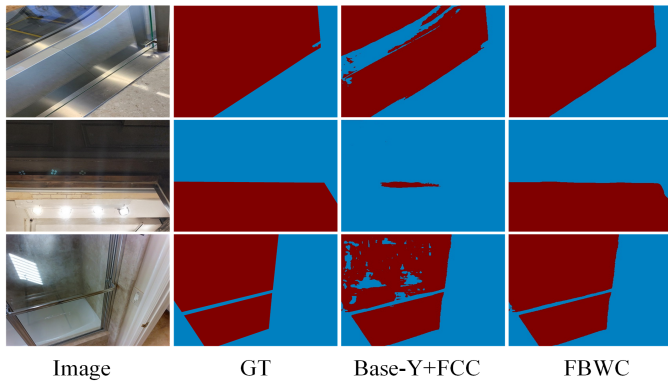


Fig. 9. Visual comparison of ablation results about CTA. Base-Y+FCC: FBWC without CTA.

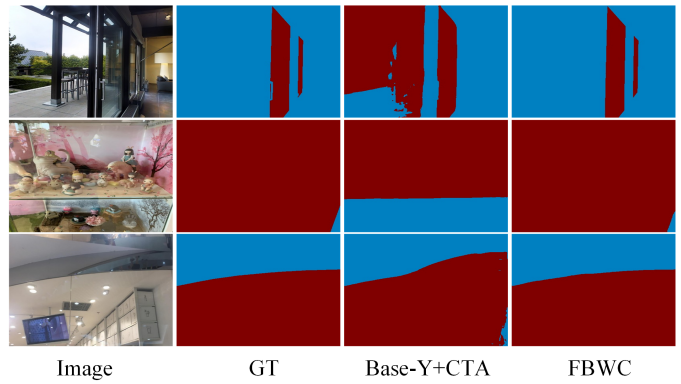


Fig. 10. Visual comparison of ablation results about FCC. Base-Y+CTA : FBWC without FCC.

TABLE IV
QUANTITATIVE ABLATION RESULTS OF CTA AND FCC. THE BASE-Y MEANS FBWC WITHOUT CTA AND FCC.

Datasets	Methods		Results		
			IoU \uparrow	MAE \downarrow	BER \downarrow
HSO	A	Base-Y + FCC	81.66	0.079	8.76
	B	Base-Y + CTA	84.07	0.079	7.61
	C	FBWC	87.59	0.059	6.27
Trans10K-stuff	A	Base-Y + FCC	83.48	0.068	6.73
	B	Base-Y + CTA	86.91	0.058	5.54
	C	FBWC	89.74	0.040	4.51
GDD	A	Base-Y + FCC	90.85	0.058	5.29
	B	Base-Y + CTA	92.79	0.037	4.29
	C	FBWC	93.17	0.035	4.03

and improving the segmentation accuracy. Visual results in Figure 10 show the importance of the FCC, which observes a sharp gradient decline of edge pixels in the conversion process of the frequency domain and spatial domain. Finally, the boundary information is integrated and strengthened to effectively divide the boundary between glass and reality.

In addition, in order to further verify the effectiveness of the proposed module, we conducted more in-depth ablation experiments on CTA and FCC. Specifically, on three datasets, we conducted three sets of ablation experiments with different

TABLE V
QUANTITATIVE ABLATION RESULTS OF FBWC WITHOUT CTA ON DIFFERENT NUMBER OF CUs. THE BASE-Z MEANS FBWC WITHOUT WCC, CTA AND FCC.

Datasets	Methods		Results	
			IoU \uparrow	MAE \downarrow
HSO	A	Base-Z + FCC + 1 CU	72.77	0.126
	B	Base-Z + FCC + 2 CUs	74.38	0.123
	C	Base-Z + FCC + 3 CUs	75.46	0.115
	D	Base-Z + FCC + 4 CUs	81.66	0.079
	E	Base-Z + FCC + 5 CUs	76.02	0.103
Trans10K-stuff	A	Base-Z + FCC + 1 CU	75.33	0.092
	B	Base-Z + FCC + 2 CUs	77.49	0.086
	C	Base-Z + FCC + 3 CUs	79.53	0.080
	D	Base-Z + FCC + 4 CUs	83.48	0.068
	E	Base-Z + FCC + 5 CUs	78.05	0.084
GDD	A	Base-Z + FCC + 1 CU	86.72	0.071
	B	Base-Z + FCC + 2 CUs	87.24	0.068
	C	Base-Z + FCC + 3 CUs	88.71	0.062
	D	Base-Z + FCC + 4 CUs	90.85	0.058
	E	Base-Z + FCC + 5 CUs	86.39	0.073

TABLE VI
QUANTITATIVE ABLATION RESULTS OF FBWC WITHOUT FCC ON DIFFERENT NUMBER OF CUs. THE BASE-Z MEANS FBWC WITHOUT WCC, CTA AND FCC.

Datasets	Methods		Results	
			IoU \uparrow	MAE \downarrow
HSO	A	Base-Z + CTA + 1 CU	75.39	0.115
	B	Base-Z + CTA + 2 CUs	77.51	0.108
	C	Base-Z + CTA + 3 CUs	78.42	0.010
	D	Base-Z + CTA + 4 CUs	84.07	0.079
	E	Base-Z + CTA + 5 CUs	80.16	0.095
Trans10K-stuff	A	Base-Z + CTA + 1 CU	76.78	0.090
	B	Base-Z + CTA + 2 CUs	78.94	0.081
	C	Base-Z + CTA + 3 CUs	82.93	0.071
	D	Base-Z + CTA + 4 CUs	86.91	0.058
	E	Base-Z + CTA + 5 CUs	81.47	0.077
GDD	A	Base-Z + CTA + 1 CU	86.97	0.069
	B	Base-Z + CTA + 2 CUs	88.76	0.062
	C	Base-Z + CTA + 3 CUs	89.39	0.056
	D	Base-Z + CTA + 4 CUs	92.79	0.037
	E	Base-Z + CTA + 5 CUs	85.82	0.077

CU numbers: FBWC without CTA, FBWC without FCC, and without both CTA and FCC. The experiment aims to further explore the effects of CTA and FCC on the segmentation accuracy of the network under different CU numbers.

It can be observed from the data shown in Table V, under GDD dataset, the network segmentation performance of the FBWC without CTA experimental group becomes better with the increase of the number of CUs, and the best advantage occurs when the number of CUs is 4. When the number of CUs is 5, the network segmentation performance decreases to 86.39% IoU and 0.073 MAE. By horizontal contrast among Table V, Table VI, and Table VII, when the number of CUs is constant, the experimental group without both CTA and FCC in FBWC performs the most poorly compared with the other two groups. To be more specific, we observed that when the number of CUs was 3 in the HSO dataset, the network segmentation results without CTA and FCC are 70.69% IoU and 0.121 MAE, which are worse than the others with the same number of CUs. At the same time, under the experimental settings above mentioned, the segmentation performance results shown in Table V and Table VII are lower than those shown in Table VI. This reflects the importance and effectiveness of the FCC in the FBWC.

The experimental phenomena mentioned above is also re-

TABLE VII
QUANTITATIVE ABLATION RESULTS OF FBWC WITHOUT CTA AND FCC ON DIFFERENT NUMBER OF CUs. THE BASE-Z MEANS FBWC WITHOUT WCC, CTA AND FCC.

Datasets	Methods		Results	
			IoU \uparrow	MAE \downarrow
HSO	A	Base-Z + 1 CU	68.92	0.130
	B	Base-Z + 2 CUs	71.33	0.118
	C	Base-Z + 3 CUs	70.69	0.121
	D	Base-Z + 4 CUs	77.41	0.093
	E	Base-Z + 5 CUs	71.84	0.116
Trans10K-stuff	A	Base-Z + 1 CU	72.71	0.150
	B	Base-Z + 2 CUs	74.25	0.120
	C	Base-Z + 3 CUs	78.43	0.092
	D	Base-Z + 4 CUs	79.92	0.090
	E	Base-Z + 5 CUs	74.81	0.100
GDD	A	Base-Z + 1 CU	82.87	0.087
	B	Base-Z + 2 CUs	83.16	0.085
	C	Base-Z + 3 CUs	84.92	0.082
	D	Base-Z + 4 CUs	86.05	0.073
	E	Base-Z + 5 CUs	81.93	0.090

flected among three datasets with different numbers of CUs. When the number of CUs is 4, the overall network can have better segmentation performance. Besides, when the proposed method CTA and FCC in the FBWC are absent, the segmentation performance will decline.

V. CONCLUSION AND FUTURE WORK

In this paper, high-precision glass segmentation is realized by strengthening the glass boundary and avoiding over-capturing semantic information in deep structure caused by the glass property of reflectivity and light transmission. We connect the designed CUs horizontally to appropriately capture large area semantic features with strong boundary constraints. Besides, CTA is embedded to keep the feature region consistent. The FCC is then utilized for the different features, which can be flexibly adjusted in a learnable way and integrated effectively. Extensive experimental results show that our proposed FBWC produces comprehensive SOTA performance on the three different public glass segmentation datasets. In the future, we will explore the application of shallow network architecture in more scenarios.

At the same time, we also objectively noted that the proposed method still has some limitations. When segmenting specific objects, as shown in Figure 11, for buildings covered by large glass groups, the network cannot effectively explore such boundaries to achieve fine and complete segmentation. Similarly, when the stained glass with decorative function is segmented, the method is susceptible to interference from the glass itself, so that the area where the glass is located cannot be accurately identified. In the future, our work will explore the application of shallow network architecture in more scenarios like buildings with large areas of glass or special glass.

ACKNOWLEDGMENT

This work was supported in part by the Natural Science Foundation of Sichuan (24NSFJQ0069), Science and Technology Service Network Initiative (KFJ-STG-QYZD-2021-21-001), the Talents by Sichuan provincial Party Committee

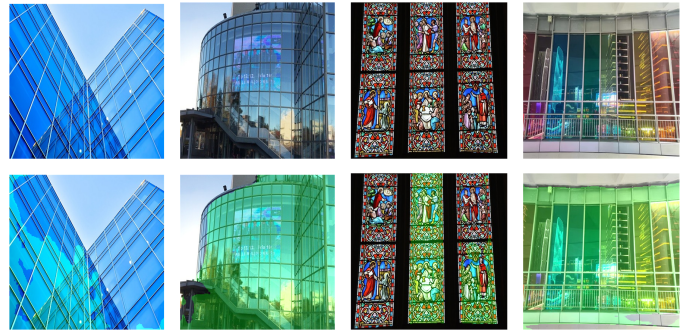


Fig. 11. Visualization of poor results of glass group and stained glass segmentation based on our works.

Organization Department, and Chengdu - Chinese Academy of Sciences Science and Technology Cooperation Fund Project (Major Scientific and Technological Innovation Projects).

REFERENCES

- [1] J. Lin, G. Wang, and R. W. Lau, "Progressive mirror detection," in *Proceedings of the IEEE/CVF Conference on Computer Vision and Pattern Recognition*, 2020, pp. 3697–3705.
- [2] J. Lin, Z. He, and R. W. Lau, "Rich context aggregation with reflection prior for glass surface detection," in *Proceedings of the IEEE/CVF Conference on Computer Vision and Pattern Recognition*, 2021, pp. 13 415–13 424.
- [3] H. He, X. Li, Y. Yang, G. Cheng, Y. Tong, L. Weng, Z. Lin, and S. Xiang, "Boundariesqueeze: Image segmentation as boundary squeezing," *arXiv preprint arXiv:2105.11668*, 2021.
- [4] C. Zheng, D. Shi, X. Yan, D. Liang, M. Wei, X. Yang, Y. Guo, and H. Xie, "Glassnet: Label decoupling-based three-stream neural network for robust image glass detection," in *Computer Graphics Forum*, vol. 41, no. 1. Wiley Online Library, 2022, pp. 377–388.
- [5] E. Xie, W. Wang, W. Wang, M. Ding, C. Shen, and P. Luo, "Segmenting transparent objects in the wild," in *Computer Vision–ECCV 2020: 16th European Conference, Glasgow, UK, August 23–28, 2020, Proceedings, Part XIII 16*. Springer, 2020, pp. 696–711.
- [6] H. He, X. Li, G. Cheng, J. Shi, Y. Tong, G. Meng, V. Prinet, and L. Weng, "Enhanced boundary learning for glass-like object segmentation," in *Proceedings of the IEEE/CVF International Conference on Computer Vision*, 2021, pp. 15 859–15 868.
- [7] Y. Cao, Z. Zhang, E. Xie, Q. Hou, K. Zhao, X. Luo, and J. Tuo, "Fakemix augmentation improves transparent object detection," *arXiv preprint arXiv:2103.13279*, 2021.
- [8] X. Li, X. Li, L. Zhang, G. Cheng, J. Shi, Z. Lin, S. Tan, and Y. Tong, "Improving semantic segmentation via decoupled body and edge supervision," in *Computer Vision–ECCV 2020: 16th European Conference, Glasgow, UK, August 23–28, 2020, Proceedings, Part XVII 16*. Springer, 2020, pp. 435–452.
- [9] H. Mei, X. Yang, Y. Wang, Y. Liu, S. He, Q. Zhang, X. Wei, and R. W. Lau, "Don't hit me! glass detection in real-world scenes," in *Proceedings of the IEEE/CVF Conference on Computer Vision and Pattern Recognition*, 2020, pp. 3687–3696.
- [10] Y. Mao, J. Yuan, Y. Zhu, and Y. Jiang, "Surface defect detection of smartphone glass based on deep learning," *The International Journal of Advanced Manufacturing Technology*, vol. 127, no. 11–12, pp. 5817–5829, 2023.
- [11] K. Wang, H. Zhang, G. Xiao, T. Wu, X. Yuan, and Y. Wang, "Attention mechanism-based feature extractor for unsupervised glass surface defect detection," in *2022 China Automation Congress (CAC)*. IEEE, 2022, pp. 2997–3002.
- [12] H. Mei, L. Yu, K. Xu, Y. Wang, X. Yang, X. Wei, and R. W. Lau, "Mirror segmentation via semantic-aware contextual contrasted feature learning," *ACM Transactions on Multimedia Computing, Communications and Applications*, vol. 19, no. 2s, pp. 1–22, 2023.
- [13] H. Guan, J. Lin, and R. W. Lau, "Learning semantic associations for mirror detection," in *Proceedings of the IEEE/CVF Conference on Computer Vision and Pattern Recognition*, 2022, pp. 5941–5950.
- [14] L. Yu, H. Mei, W. Dong, Z. Wei, L. Zhu, Y. Wang, and X. Yang, "Progressive glass segmentation," *IEEE Transactions on Image Processing*, vol. 31, pp. 2920–2933, 2022.

- [15] X. Hu, R. Gao, S. Yang, and K. Cho, "Tgsnet: Multi-field feature fusion for glass region segmentation using transformers," *Mathematics*, vol. 11, no. 4, p. 843, 2023.
- [16] G. R. Hu, Xiaohang, S. Yang, and K. Cho, "Cagnet: A multi-scale convolutional attention method for glass detection based on transformer," *Mathematics*, vol. 11, no. 19, p. 4084, 2023.
- [17] X. Hou, M. Zhan, C. Wang, and C. Fan, "Glass objects detection based on transformer encoder-decoder," in *2022 6th International Conference on Automation, Control and Robots (ICACR)*. IEEE, 2022, pp. 217–223.
- [18] J. Lin, Y.-H. Yeung, and R. Lau, "Exploiting semantic relations for glass surface detection," *Advances in Neural Information Processing Systems*, vol. 35, pp. 22490–22504, 2022.
- [19] C. Tang, L. Xu, B. Yang, Y. Tang, and D. Zhao, "Gru-based interpretable multivariate time series anomaly detection in industrial control system," *Computers & Security*, vol. 127, p. 103094, 2023.
- [20] J. Ba and R. Caruana, "Do deep nets really need to be deep?" *Advances in neural information processing systems*, vol. 27, 2014.
- [21] M. Tan and Q. Le, "Efficientnet: Rethinking model scaling for convolutional neural networks," in *International conference on machine learning*. PMLR, 2019, pp. 6105–6114.
- [22] Z. Chen, Q. Xu, R. Cong, and Q. Huang, "Global context-aware progressive aggregation network for salient object detection," in *Proceedings of the AAAI conference on artificial intelligence*, vol. 34, no. 07, 2020, pp. 10599–10606.
- [23] C. P. Chen and Z. Liu, "Broad learning system: An effective and efficient incremental learning system without the need for deep architecture," *IEEE transactions on neural networks and learning systems*, vol. 29, no. 1, pp. 10–24, 2017.
- [24] R. Xie and S. Wang, "Downsizing and enhancing broad learning systems by feature augmentation and residuals boosting," *Complex & Intelligent Systems*, vol. 6, no. 2, pp. 411–429, 2020.
- [25] Z. Liu, C. P. Chen, S. Feng, Q. Feng, and T. Zhang, "Stacked broad learning system: From incremental flattened structure to deep model," *IEEE Transactions on Systems, Man, and Cybernetics: Systems*, vol. 51, no. 1, pp. 209–222, 2020.
- [26] R. Xie, C.-M. Vong, C. P. Chen, and S. Wang, "Dynamic network structure: Doubly stacking broad learning systems with residuals and simpler linear model transmission," *IEEE Transactions on Emerging Topics in Computational Intelligence*, vol. 6, no. 6, pp. 1378–1395, 2022.
- [27] X. Zhang, T. Wang, J. Qi, H. Lu, and G. Wang, "Progressive attention guided recurrent network for salient object detection," in *Proceedings of the IEEE conference on computer vision and pattern recognition*, 2018, pp. 714–722.
- [28] S. Shi, R. Yang, and H. You, "A new two-dimensional fourier transform algorithm based on image sparsity," in *2017 IEEE international conference on acoustics, speech and signal processing (ICASSP)*. IEEE, 2017, pp. 1373–1377.
- [29] D.-P. Fan, G.-P. Ji, T. Zhou, G. Chen, H. Fu, J. Shen, and L. Shao, "Pranet: Parallel reverse attention network for polyp segmentation," in *International conference on medical image computing and computer-assisted intervention*. Springer, 2020, pp. 263–273.
- [30] O. Ronneberger, P. Fischer, and T. Brox, "U-net: Convolutional networks for biomedical image segmentation," in *Medical image computing and computer-assisted intervention—MICCAI 2015: 18th international conference, Munich, Germany, October 5–9, 2015, proceedings, part III 18*. Springer, 2015, pp. 234–241.
- [31] Y. Zhang, H. Liu, and Q. Hu, "Transfuse: Fusing transformers and cnns for medical image segmentation," in *Medical Image Computing and Computer Assisted Intervention—MICCAI 2021: 24th International Conference, Strasbourg, France, September 27–October 1, 2021, Proceedings, Part I 24*. Springer, 2021, pp. 14–24.
- [32] Q. Hou, M.-M. Cheng, X. Hu, A. Borji, Z. Tu, and P. H. Torr, "Deeply supervised salient object detection with short connections," in *Proceedings of the IEEE conference on computer vision and pattern recognition*, 2017, pp. 3203–3212.
- [33] N. Liu, J. Han, and M.-H. Yang, "Picanet: Learning pixel-wise contextual attention for saliency detection," in *Proceedings of the IEEE conference on computer vision and pattern recognition*, 2018, pp. 3089–3098.
- [34] S. Chen, X. Tan, B. Wang, and X. Hu, "Reverse attention for salient object detection," in *Proceedings of the European conference on computer vision (ECCV)*, 2018, pp. 234–250.
- [35] Z. Wu, L. Su, and Q. Huang, "Cascaded partial decoder for fast and accurate salient object detection," in *Proceedings of the IEEE/CVF conference on computer vision and pattern recognition*, 2019, pp. 3907–3916.
- [36] J.-X. Zhao, J.-J. Liu, D.-P. Fan, Y. Cao, J. Yang, and M.-M. Cheng, "Egnet: Edge guidance network for salient object detection," in *Proceedings of the IEEE/CVF international conference on computer vision*, 2019, pp. 8779–8788.
- [37] J. Wei, S. Wang, and Q. Huang, "F³net: fusion, feedback and focus for salient object detection," in *Proceedings of the AAAI conference on artificial intelligence*, vol. 34, no. 07, 2020, pp. 12321–12328.
- [38] Y. Pang, X. Zhao, L. Zhang, and H. Lu, "Multi-scale interactive network for salient object detection," in *Proceedings of the IEEE/CVF conference on computer vision and pattern recognition*, 2020, pp. 9413–9422.
- [39] H. Zhou, X. Xie, J.-H. Lai, Z. Chen, and L. Yang, "Interactive two-stream decoder for accurate and fast saliency detection," in *Proceedings of the IEEE/CVF conference on computer vision and pattern recognition*, 2020, pp. 9141–9150.
- [40] J. Wei, S. Wang, Z. Wu, C. Su, Q. Huang, and Q. Tian, "Label decoupling framework for salient object detection," in *Proceedings of the IEEE/CVF conference on computer vision and pattern recognition*, 2020, pp. 13025–13034.
- [41] X. Qin, Z. Zhang, C. Huang, M. Dehghan, O. R. Zaiane, and M. Jagersand, "U2-net: Going deeper with nested u-structure for salient object detection," *Pattern recognition*, vol. 106, p. 107404, 2020.
- [42] H. Zhao, X. Qi, X. Shen, J. Shi, and J. Jia, "Icnet for real-time semantic segmentation on high-resolution images," in *Proceedings of the European conference on computer vision (ECCV)*, 2018, pp. 405–420.
- [43] H. Zhao, J. Shi, X. Qi, X. Wang, and J. Jia, "Pyramid scene parsing network," in *Proceedings of the IEEE conference on computer vision and pattern recognition*, 2017, pp. 2881–2890.
- [44] L.-C. Chen, G. Papandreou, I. Kokkinos, K. Murphy, and A. L. Yuille, "Deeplab: Semantic image segmentation with deep convolutional nets, atrous convolution, and fully connected crfs," *IEEE transactions on pattern analysis and machine intelligence*, vol. 40, no. 4, pp. 834–848, 2017.
- [45] M. Yang, K. Yu, C. Zhang, Z. Li, and K. Yang, "Denseaspp for semantic segmentation in street scenes," in *Proceedings of the IEEE conference on computer vision and pattern recognition*, 2018, pp. 3684–3692.
- [46] C. Yu, J. Wang, C. Peng, C. Gao, G. Yu, and N. Sang, "Bisenet: Bilateral segmentation network for real-time semantic segmentation," in *Proceedings of the European conference on computer vision (ECCV)*, 2018, pp. 325–341.
- [47] J. Fu, J. Liu, H. Tian, Y. Li, Y. Bao, Z. Fang, and H. Lu, "Dual attention network for scene segmentation," in *Proceedings of the IEEE/CVF conference on computer vision and pattern recognition*, 2019, pp. 3146–3154.
- [48] Z. Huang, X. Wang, L. Huang, C. Huang, Y. Wei, and W. Liu, "Ccnnet: Criss-cross attention for semantic segmentation," in *Proceedings of the IEEE/CVF international conference on computer vision*, 2019, pp. 603–612.
- [49] X. Li, H. Zhao, L. Han, Y. Tong, S. Tan, and K. Yang, "Gated fully fusion for semantic segmentation," in *Proceedings of the AAAI conference on artificial intelligence*, vol. 34, no. 07, 2020, pp. 11418–11425.
- [50] X. Li, A. You, Z. Zhu, H. Zhao, M. Yang, K. Yang, S. Tan, and Y. Tong, "Semantic flow for fast and accurate scene parsing," in *Computer Vision—ECCV 2020: 16th European Conference, Glasgow, UK, August 23–28, 2020, Proceedings, Part I 16*. Springer, 2020, pp. 775–793.
- [51] S. Huang, Z. Lu, R. Cheng, and C. He, "Fapn: Feature-aligned pyramid network for dense image prediction," in *Proceedings of the IEEE/CVF international conference on computer vision*, 2021, pp. 864–873.
- [52] J. Xu, Z. Xiong, and S. P. Bhattacharyya, "Pidnet: A real-time semantic segmentation network inspired by pid controllers," in *Proceedings of the IEEE/CVF conference on computer vision and pattern recognition*, 2023, pp. 19529–19539.
- [53] X. Hu, L. Zhu, C.-W. Fu, J. Qin, and P.-A. Heng, "Direction-aware spatial context features for shadow detection," in *Proceedings of the IEEE conference on computer vision and pattern recognition*, 2018, pp. 7454–7462.
- [54] Q. Zheng, X. Qiao, Y. Cao, and R. W. Lau, "Distraction-aware shadow detection," in *Proceedings of the IEEE/CVF conference on computer vision and pattern recognition*, 2019, pp. 5167–5176.
- [55] L. Zhu, Z. Deng, X. Hu, C.-W. Fu, X. Xu, J. Qin, and P.-A. Heng, "Bidirectional feature pyramid network with recurrent attention residual modules for shadow detection," in *Proceedings of the European Conference on Computer Vision (ECCV)*, 2018, pp. 121–136.
- [56] D.-P. Fan, G.-P. Ji, G. Sun, M.-M. Cheng, J. Shen, and L. Shao, "Camouflaged object detection," in *Proceedings of the IEEE/CVF conference on computer vision and pattern recognition*, 2020, pp. 2777–2787.

- [57] H. Mei, G.-P. Ji, Z. Wei, X. Yang, X. Wei, and D.-P. Fan, "Camouflaged object segmentation with distraction mining," in *Proceedings of the IEEE/CVF conference on computer vision and pattern recognition*, 2021, pp. 8772–8781.
- [58] Y. Lv, J. Zhang, Y. Dai, A. Li, B. Liu, N. Barnes, and D.-P. Fan, "Simultaneously localize, segment and rank the camouflaged objects," in *Proceedings of the IEEE/CVF Conference on Computer Vision and Pattern Recognition*, 2021, pp. 11 591–11 601.
- [59] X. Yang, H. Mei, K. Xu, X. Wei, B. Yin, and R. W. Lau, "Where is my mirror?" in *Proceedings of the IEEE/CVF International Conference on Computer Vision*, 2019, pp. 8809–8818.
- [60] E. Xie, W. Wang, W. Wang, P. Sun, H. Xu, D. Liang, and P. Luo, "Segmenting transparent object in the wild with transformer," *arXiv preprint arXiv:2101.08461*, 2021.
- [61] K. Fan, C. Wang, Y. Wang, C. Wang, R. Yi, and L. Ma, "Rfenet: towards reciprocal feature evolution for glass segmentation," in *Proceedings of the Thirty-Second International Joint Conference on Artificial Intelligence*, ser. IJCAI '23, 2023. [Online]. Available: <https://doi.org/10.24963/ijcai.2023/80>



Fei Zhu received the B.E. degree in mechanical engineering from Tsinghua University, China, in 2018, and the Ph.D. degree in pattern recognition and intelligent systems from the Institute of Automation, Chinese Academy of Sciences, China, in 2023. He is now a postdoctoral fellow at the Centre for Artificial Intelligence and Robotics, Hong Kong Institute of Science & Innovation, Chinese Academy of Sciences. His research interests include open-world and trustworthy machine learning.



Zhang Yi (Fellow, IEEE) received the Ph.D. degree in mathematics from the Institute of Mathematics, Chinese Academy of Sciences, China, in 1994. He is currently a Professor with the College of Computer Science, Sichuan University, China. He coauthored three books entitled *Convergence Analysis of Recurrent Neural Networks* (Kluwer, 2004), *Neural Networks: Computational Models and Applications* (Springer, 2007), and *Subspace Learning of Neural Networks* (CRC, 2010). His research interests include neural networks and intelligent medicine. He

was an Associate Editor for IEEE TRANSACTIONS ON CYBERNETICS. From 2009 to 2012, he was an Associate Editor for IEEE TRANSACTIONS ON NEURAL NETWORKS AND LEARNING SYSTEMS. He is a Foreign Member of Russian Academy of Engineering.



Xiaolin Qin (Senior Member, IEEE) is a Professor in Chengdu Institute of Computer Applications, Chinese Academy of Sciences and University of Chinese Academy of Sciences, China. Qin received his Ph.D. degree in July 2011. From May 2014 to June 2015, he was a postdoctoral fellow at Department of Computer and Information Science, Linköping University, Sweden. His research interests include automated reasoning and algebraic vision.



Jiachen Liu is a research assistant of Chengdu Institute of Computer Applications at Chinese Academy of Sciences, China. Liu received his Postgraduate degree in June 2024 from Kunming University of Science and Technology. His research interests include image processing and algebraic vision.



Qianlei Wang received the M.S. degree in Computer Application from Civil Aviation Flight University of China, China, in July 2022. He is currently working toward the Ph.D. degree with the School of Computer Science and Technology at University of Chinese Academy of Sciences, China. His research interests include SLAM and algebraic vision.



Shaolin Zhang is currently working toward the Ph.D. degree with the School of Computer Science and Technology at University of Chinese Academy of Sciences, China. He received his PostGraduate degree in July 2023 from Chongqing University of Science and Technology, China. His research interests include image processing and monocular depth estimation.